Local electronic transport at grain boundaries in Nb-doped $SrTiO_3$

Sergei V. Kalinin[1] and Dawn A. Bonnell[2]
[1]*Condensed Matter Sciences Division, Oak Ridge National Laboratory, Oak Ridge, Tennessee 37831, USA*
[2]*Department of Materials Science and Engineering, The University of Pennsylvania, 3231 Walnut St, Philadelphia, Pennsylvania 19104, USA*
(Received 3 January 2004; revised manuscript received 6 August 2004; published 2 December 2004)

The local electrostatic properties and electronic transport at $\Sigma 5$ grain boundaries in donor-doped $SrTiO_3$ bicrystals are examined using a combination of scanning probe microscopy (SPM) techniques and impedance spectroscopy. A combination of scanning surface potential microscopy (SSPM) and scanning impedance microscopy is used to determine intrinsic current-voltage and capacitance-voltage characteristics of the interface, eliminating the bulk and contact contributions. Conductive atomic force microscopy is used to directly image the depletion barrier associated with the grain boundary. The sign of the grain boundary potential is unambiguously determined by SSPM once the mobile charge effect is taken into account. A combination of SPM and impedance spectroscopy allowed the effect of grain boundary on local static and frequency dependent transport properties to be established.

DOI: 10.1103/PhysRevB.70.235304 PACS number(s): 73.40.−c, 68.47.Gh, 77.84.−s, 68.37.Ps

I. INTRODUCTION

The interplay between structure, charge, orbital and spin degrees of freedom in oxides gives rise to semiconducting,[1] dielectric,[2] ferroelectric,[3,4] superconducting,[5] and magnetoresistive[6,7] properties. The majority of experimental studies and applications of oxides are based on polycrystalline bulk or thin film materials characterized by the presence of a large number of grain boundaries between regions with dissimilar crystallographic orientation. Grain boundaries often enable useful behavior, such as low-field magnetoresistance,[8–11] grain boundary Josephson junctions,[12] positive temperature coefficient of resistivity[13,14] and varistor behavior.[15] In other cases, interfaces limit the performance of the material, e.g., critical current density in high temperature superconductors. Grain boundary transport is usually governed by the electronic properties of the interface such as interface charge and depletion width, even though more subtle effects associated with magnetic disorder, strain and order parameter mismatch are possible.

Fundamental insights into the physics of grain boundary phenomena come from structure-property relations at well-defined coherent interfaces, for which the structure is unique and electronic, and structural and transport measurements can be correlated with theoretical studies. The perovskite $SrTiO_3$ is a prototype oxide in which the presence of interface charge results in grain boundary potential barriers. The local properties of grain boundaries in $SrTiO_3$ on an atomic level have been extensively studied by high resolution transmission electron microscopy (HRTEM), scanning transmission electron microscopy (STEM), electron energy loss spectroscopy, electron holography,[16–20] and are the subject of intensive theoretical studies.[21,22]

Despite extensive effort, little is known about the origin of the potential barrier at the interface and hence the fundamental relationships between the atomic structure of the interface and its electric properties. In several cases, this was addressed using the combination of high resolution HRTEM and STEM studies with transport measurements such as current-voltage (I-V), capacitance voltage (C-V) and impedance spectroscopy, from which the potential barrier height at the interface, interface charge and depletion width can be determined.[23] In the last several years, a number of approaches were developed for spatially resolved transport measurements at electroactive interfaces using electron holography and scanning probe microscopy. The energy resolution in electron beam based techniques generally does not exceed 0.5 eV and they are limited to the determination of static properties of the interfaces and direct current transport. Thus, scanning probe microscopy techniques that provide the information on static and frequency dependent transport properties with high energy (~mV) and spatial resolution complementary to the structural data from HRTEM and STEM are expected to provide new horizons in our understanding of structure-electronic property relationships at electroactive interfaces.

In the present paper, scanning probe microscopy (SPM) is used to study the potential barrier and lateral transport at an electroactive $\Sigma 5$ grain boundary in semiconducting, Nb-doped $SrTiO_3$. Scanning surface potential microscopy (SSPM) on a grounded surface is used to localize the grain boundary. SSPM on the laterally biased surface is used to determine local I-V characteristics of the interface. Scanning impedance microscopy (SIM) is used to determine local, frequency-dependent transport properties and interface resistance and capacitance. A number of models for the analysis of frequency-dependent interface properties from SIM data are developed. This allowed the direct measurement of voltage-dependent, intrinsic grain boundary resistance and capacitance, excluding the contact and bulk contributions. Direct insight into the electronic properties of the grain boundary is obtained using conductive atomic force microscopy (c-AFM) to image the depletion barrier associated with the grain boundary.

II. SPM ANALYSIS OF GRAIN BOUNDARY TRANSPORT

Given the early stage of the development of SPM as applied to interface transport, we present the basic principles of

 ©2004 The American Physical Society

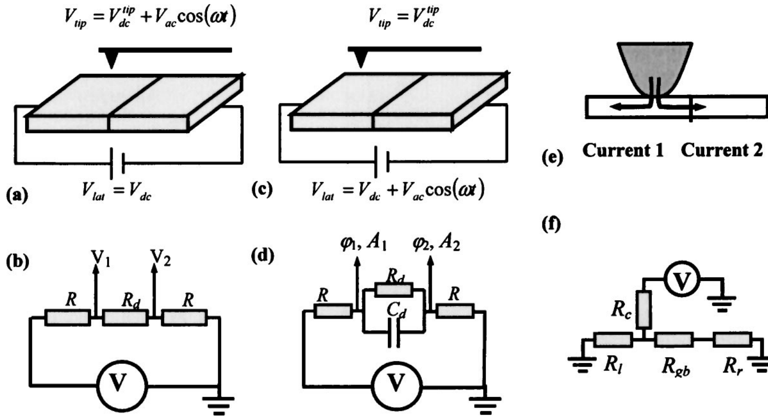

FIG. 1. Schematic diagram (a), (c), (e) and corresponding equivalent circuit (b), (d), (f) of scanning surface potential microscopy (a), (b), scanning impedance microscopy (c), (d) and conductive AFM (e), (f).

the technique prior to a discussion of the application to quantitative studies of transport behavior. The quantitative basis of direct current measurements by SSPM is summarized in Sec. II A; an approach for frequency dependent transport measurements by SIM and corresponding theoretical analysis are presented in Sec. II B; and direct imaging of grain boundary space charge barrier and transport measurements by conductive AFM are summarized in Sec. II C.

A. Direct current transport measurements by SSPM

Scanning surface potential microscopy[24,25] is based on dual pass imaging. Electrostatic data are collected 50–100 nm above the surface during second (interleaved) scan as illustrated in Fig. 1(a). In SSPM the tip is biased directly by $V_{\mathrm{tip}}=V_{\mathrm{dc}}+V_{\mathrm{ac}}\cos(\omega t)$, where V_{ac} is referred to as the driving voltage. The first harmonic of the capacitive force acting on a tip is

$$F_{1\omega}^{\mathrm{cap}}(z) = C_z'(V_{\mathrm{dc}} - V_s)V_{\mathrm{ac}}, \tag{1}$$

where C_z' is the tip-surface capacitance gradient, z is the tip-surface separation and V_s is the surface potential. Feedback is used to nullify $F_{1\omega}^{\mathrm{cap}}$ by adjusting the dc component of tip bias, and mapping the nulling potential V_{dc} yields a surface potential map, $V_s=V_{\mathrm{e}\ell}+\Delta CPD$, where $V_{\mathrm{e}\ell}$ is the electrostatic potential of the surface and ΔCPD is the contact potential difference between the tip and the surface.

On the grounded surface, SSPM directly measures the local work function, ΔCPD. The presence of localized charges at the interfaces will result in a potential variation above the grain boundary, and several SSPM studies of electroactive interfaces on grounded surfaces have been reported.[26,27] It is recognized that SSPM measures the potential distribution above the surface, rather than in the bulk, and a numerical procedure to relate the two was suggested by Kalinin and Bonnell.[28] However, surface screening by mobile surface charges[29,30] can significantly affect the surface potential, resulting in a significant lowering of the measured potential and even an erroneous determination of the sign of grain boundary charge. Some of these issues are addressed in Sec. IV A. Despite this, SSPM on grounded surfaces allows unambiguous localization of the electroactive interface.

In a SSPM transport experiment, a biased interface is connected to a voltage source in series with current-limiting resistors to prevent accidental current flow to the tip. For such a circuit, shown in Fig. 1(b), the total resistivity of the sample R_Σ is

$$R_\Sigma = 2R + R_{\mathrm{gb}}(V_{\mathrm{gb}}), \tag{2}$$

where V_{gb} is the potential across the interface, $R_{\mathrm{gb}}(V_{\mathrm{gb}})$ is the voltage dependent resistivity of the interface, and R is the resistivity of the external current-limiting resistors.

The applied bias dependence of the potential drop at the interface is directly measured by SSPM and is referred to as the voltage characteristics of the interface. In the general case, interface current-voltage characteristics, $I_{\mathrm{gb}}(V_{\mathrm{gb}})$, can be reconstructed as

$$I_{\mathrm{gb}}(V_{\mathrm{gb}}) = (V - V_{\mathrm{gb}})/2R \tag{3}$$

for the known values of the current-limiting resistors. A variation in the current-limiting resistance, R, can be used to determine the presence of stray resistances in the circuit (e.g., contact and bulk resistances). Alternatively, the current, I_{gb}, can be measured directly using a current-voltage converter. Thus, SSPM of laterally biased devices is similar to the conventional four probe resistance measurements, in which the SPM tip acts as a moving voltage probe providing the spatially resolved potential data.

SSPM metrology of laterally biased devices is limited by a significant cantilever contribution to the measured potential, minimization of which requires imaging at small tip-surface separations.[31] To compensate for potential variations due to differences in local work function, images under applied lateral bias are corrected by the surface potential values measured for the grounded surface.

B. Frequency dependent transport measurements by SIM

Similar to SSPM, scanning impedance microscopy is based on dual pass imaging. In SIM, the tip is held at constant bias V_{dc} and a lateral bias $V_{\ell\mathrm{at}}=V_{\mathrm{dc}}+V_{\mathrm{ac}}\cos(\omega t)$, is applied across the sample [Fig. 1(c)]. This lateral bias induces oscillations in the surface potential

$$V_{\mathrm{surf}} = V_s + V_{\mathrm{ac}}(x)\cos[\omega t + \varphi(x)], \tag{4}$$

where $\varphi(x)$ and $V_{\mathrm{ac}}(x)$ are the position dependent phase shift and voltage oscillation amplitude and V_s is the dc surface potential. Oscillations in surface potential induce the me-

TABLE I. Frequency dependence of interface phase shift and amplitude ratio.

Frequency, ω	Phase shift, $\tan(\varphi_{gb})$	Amplitude ratio, A_1/A_2
Low frequency limit, $\omega \ll \omega_r$	$\omega C_{gb} R_{gb}^2 / (R+R_{gb})$	$(R+R_{gb})/R$
High frequency limit, $\omega \ll \omega_r$	$1/\omega C_{gb} R$	1
Crossover frequency, $\omega_r = R_{gb}^{-1} C_{gb}^{-1} \sqrt{1+R_{gb}/R}$	$R_{gb}/2\sqrt{R(R+R_{gb})}$	$\sqrt{(R+R_{gb})/R}$

chanical vibration of a dc biased tip. Far from the resonant frequency of the cantilever, the phase lag between the phase of the surface voltage oscillations and mechanical tip oscillations is position independent, while the mechanical oscillation amplitude $A(\omega)$ is proportional to the local voltage oscillation amplitude $V_{ac}(x)$. Therefore, variation in the phase shift (phase image) of cantilever oscillations along the surface is equal to the variation of the voltage phase shift with a (frequency dependent) offset due to the inertia between the sample and tip. The tip oscillation amplitude is proportional to the local voltage oscillation amplitude and constitutes the SIM amplitude image.

To include the correction for the variation of potential and work function across the surface, the voltage amplitude ratio is calculated from experimental tip oscillation amplitudes and SSPM data acquired at the same dc bias conditions as

$$\frac{A_1}{A_2} = \frac{A_1^{sim}(V_{tip}^{dc} - V_2)}{A_2^{sim}(V_{tip}^{dc} - V_1)}, \quad (5)$$

where A_1^{sim} and A_2^{sim} are the amplitude signals to the left and right of the interface, V_{tip}^{dc} is the dc tip bias during SIM and V_1 and V_2 are the surface potentials to the left and right of the interface determined by SSPM.

For a single interface device the analysis of the SIM imaging mechanism is similar to that of SSPM. For the equivalent circuit in Fig. 1(d) the total impedance of the circuit, Z_Σ, is $Z_\Sigma = 2R + Z_{gb}$, where Z_{gb} is the grain boundary impedance. The grain boundary equivalent circuit is represented by a parallel R-C element and the impedance is $Z_{gb}^{-1} = R_{gb}^{-1} + i\omega C_{gb}$, where R_{gb} and C_{gb} are the voltage dependent interface resistance and capacitance. Experimentally accessible and independent of tip properties are the interface phase shift, $\varphi_{gb} = \varphi_2 - \varphi_1$, and amplitude ratio, A_1/A_2, across the interface. The interface phase shift is calculated from the ratio of impedances from each side of the interface, $\beta = R/(Z_{gb}+R)$, as $\tan(\varphi_{gb}) = \mathrm{Im}(\beta)/\mathrm{Re}(\beta)$ (impedance divider effect). For the equivalent circuit in Fig. 1(d)

$$\tan(\varphi_d) = \frac{\omega C_d R_d^2}{(R + R_d) + R\omega^2 C_d^2 R_d^2}. \quad (6)$$

The voltage oscillation amplitude ratio, $A_1/A_2 = |\beta|^{-1}$, is

$$\beta^{-2} = \frac{\{(R + R_d) + R\omega^2 C_d^2 R_d^2\}^2 + \omega^2 C_d^2 R_d^4}{R^2(1 + \omega^2 C_d^2 R_d^2)^2}. \quad (7)$$

High and low frequency limiting behavior for Eqs. (6) and (7) is summarized in Table I. In the high frequency limit, a phase shift at the interface is determined by the interface capacitance and circuit termination only. Thus, SIM phase imaging at frequencies *above* the interface relaxation frequency, $\omega \gg \omega_r = R_{gb}^{-1} C_{gb}^{-1}$, provides a quantitative measure of interface capacitance. Quantitative determination of the interface C-V curve for a metal-semiconductor interface using a combination of SIM in the high frequency regime and SSPM was reported elsewhere.[32]

Similar to conventional impedance spectroscopy,[33] the interface phase shift and the amplitude ratio are complementary and can be used to determine the interface transport properties. For frequency independent R_{gb}, C_{gb} (Model 1), experimental phase shift frequency [Model 1(a)], amplitude ratio frequency [Model 1(b)] or both data sets [Model 1(c)] can be fitted to Eqs. (6) and (7), where C_{gb} and R_{gb} are now fitting parameters and R is a known circuit termination. For models 1(a) and (b), the second observable provides independent verification of the results. Alternatively, frequency dependent interface resistance and capacitance $R_{gb}(\omega)$, $C_{gb}(\omega)$ (Model 2) can be calculated for each frequency from the experimental phase shift and amplitude ratio. Such data are expected to be particularly important for the characterization of interfaces with a large frequency dispersion in interface transport properties, e.g., due to the interface states or deep traps at semiconductor grain boundaries[34] or to several relaxation processes in ionic conductors, for which interpretation of conventional impedance spectroscopy results is not straightforward.

C. Conductive AFM

In conductive AFM, or scanning spreading resistance microscopy, the dc current through the tip-surface junction under applied bias is measured.[35–37] Formation of depletion regions in the vicinity of a grain boundary is associated with a decrease of local carrier concentration and an increase of the tip-surface spreading resistance, $R_{sp} = 1/4\sigma a$, where σ is local conductivity and a is contact radius. Thus, the grain boundary is associated with a low conductivity region in the c-AFM image. However, quantitative interpretation of c-AFM images in terms of local carrier concentration is not straightforward, since both tip-surface contact resistance and spreading resistance depend on carrier concentration in the material. Additional difficulties arise due to tip-induced band bending and conductive water layers on the surface.[30] Nevertheless, similar to SSPM on grounded surfaces, c-AFM can be used to localize depletion-type grain boundaries.

An alternative approach to local transport measurements using c-AFM that minimizes contact resistance effects employs a two-terminal configuration as illustrated in Fig. 1(e).[38] In two-terminal c-AFM, the current on the left contact, I_ℓ, and the right contact, I_r, induced by current, I_t, injected from the biased tip, are measured. From charge conservation, $I_t = I_\ell + I_r$. From the equivalent circuit in Fig. 1(f), for a symmetric crystal ($R_\ell = R_r = R$), the currents are

$$I_\ell = V_{\text{tip}} \frac{(R_{\text{gb}} + R)}{R^2 + R_{\text{gb}} R_{\text{ts}} + R(R_{\text{gb}} + 2R_{\text{ts}})}, \tag{8a}$$

$$I_r = V_{\text{tip}} \frac{R}{R^2 + R_{\text{gb}} R_{\text{ts}} + R}. \tag{8b}$$

For a good tip-surface contact, $R_{\text{ts}} \ll R_{\text{gb}}$, and Eqs. (8a) and (8b) are simplified as $I_\ell = V_{\text{tip}}/R$, and $I_\ell = V_{\text{tip}}/(R + R_{\text{gb}})$. The ratio of currents on the left and right are independent of tip-surface contact resistance and can be calculated as

$$\frac{I_\ell}{I_r} = \frac{R}{R + R_{\text{gb}}}. \tag{9}$$

Thus, Eq. (9) can be used to determine grain boundary resistance and bulk resistances from two-terminal c-AFM data. The characteristic width of single- and two-terminal c-AFM profiles provides an upper estimate on the thickness of the depletion layers at the interface.

III. EXPERIMENTAL PROCEDURE

In order to relate the grain boundary properties to atomic configuration, an interface with a known structure was used. Nb-doped, $\Sigma 5$ $SrTiO_3$ bicrystals (1 at. %) were produced by diffusion bonding. A $10 \times 10 \times 0.5$ mm crystal, dark blue due to the donor doping, is sectioned such that the grain boundary is perpendicular to the (100) surface. Numerous high resolution transmission electron microscopy studies on this and similar bicrystals have shown that the interfaces are atomically abrupt, with no impurity segregation.[39,40] To study the static and frequency dependent transport, bicrystals were soldered by indium to copper contact pads. An additional pair of indium contacts was fabricated for four probe transport measurements.

The AFM, SSPM, SIM and c-AFM measurements were performed on a commercial instrument (Digital Instruments Dimension 3000 NS-IIIA) using a variety of probes. The lift height for the interleave scans[41] in the SSPM and SIM was usually 100 nm. Measurements were performed using Au coated cantilevers (spring constant $k = 1-5$ N/m, NCSC 12 Cr-Au, Micromasch). The scan rate varied from 0.5 Hz for large scans (~ 80 μm) to 1 Hz for smaller scans (~ 10 μm). The driving voltage V_{ac} in the interleave scan was 5 V for the SSPM and 1 V_{pp} for the SIM. The scan rate varied from 0.2 to 0.5 Hz. To reduce the effect of drift the images were acquired with the grain boundary oriented along the slow scan axis. SSPM images were processed with a constant background subtraction. To quantify the dc transport properties of the interface, the tip was repeatedly scanned along the same line across the surface and a slow ($\sim$mHz) triangular voltage ramp was applied across the boundary. The resulting image represents potential profiles at different lateral biases, from which voltage characteristics of the interface can be determined.

For SIM measurements, the microscope was equipped with a function generator and lock-in amplifier (DS340, SRS 830, Stanford Research Systems) as described elsewhere.[32] To quantify the frequency and bias dependence of interface capacitance, numerous SIM images were collected for varying lateral biases and driving frequencies. Circuit termination resistors in SSPM and SIM were varied from 500 Ω to 1 MΩ.

To perform single-terminal and two-terminal conductive AFM measurements, the microscope was additionally equipped with Ithaco current amplifiers and a custom-built current-voltage converter (Current Designs, Inc). Measurements were performed using Co-Cr coated cantilevers (spring constant $k = 1$ N/m, MESP, Digital Instruments); gold-coated cantilevers were found to produce inferior contact to the surface and the current imaging was unstable. Collected was tip-surface current (single-terminal measurements) and currents on the left and right contacts (two-terminal measurements).

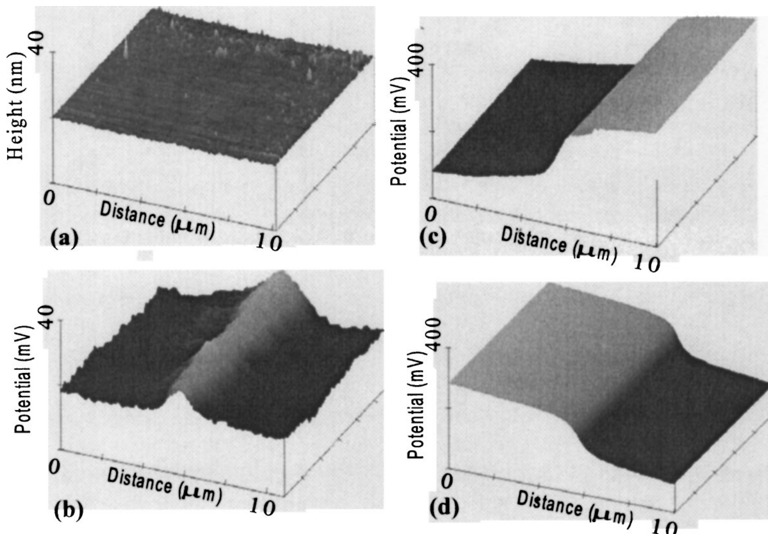

FIG. 2. Surface topography (a), surface potential of the grounded surface (b) and surface potential for forward (c) and reverse (d) bias. The scale for (b) is 40 mV and for (c), (d) is 400 mV.

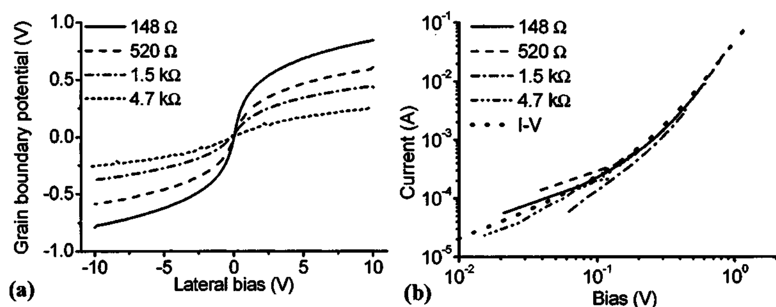

FIG. 3. (a) Interface potential drop as a function of external lateral bias for different current limiting resistors and (b) *I-V* curve reconstruction from SSPM data compared to two-probe *I-V* measurements.

Frequency dependent transport properties were measured by impedance spectroscopy (HP4282A *LCR* meter) in the frequency range 20 Hz–1 MHz with a modulation signal of 20 mV. In addition, variable temperature impedance spectroscopy and four probe *I-V* measurements were performed as described elsewhere.[42]

IV. RESULTS AND DISCUSSION

A. Surface potential of the grounded surface

The structural origins of electrical activity of the grain boundary can be addressed by direct measurement of the magnitude and sign of local potential on the grounded surface as related to the structure of the grain boundary. The structure of the $\Sigma 5$ boundary viewed in the (100) plane cross section consists of two alternating pentagonal oxygen structural units containing two Sr columns and two Ti columns, respectively.[16–19] In both units the cation positions are half occupied, forming a grain boundary reconstruction.[43,44] A stoichiometric grain boundary is neutral in terms of formal charge. For an oxygen deficient grain boundary, the Ti will be partially reduced and the interface carries formal charge compensated by free carriers in an adjacent space charge region. Atomically resolved EELS measurements have confirmed the presence of Ti^{3+} cations at the interface.[39] However, the exact occupation of the cation columns cannot be determined from the STEM data and minute deviations from exact cation or oxygen stoichiometry can result in large interface charges. These structural results *per se*, therefore, cannot address the origin and nature of grain boundary states and the sign of interface charge.

To facilitate the interpretation of SSPM data on the grounded and biased surfaces, we briefly discuss the relationship between grain boundary potential and electrical properties. A negatively charged grain boundary in the donor-doped material is associated with depletion regions, resulting in a lower carrier concentration in the vicinity of the interface. A depleted grain boundary is highly resistive, primary transport mechanisms being thermionic emission and diffusion across the double Schottky barrier. A positively charged grain boundary is associated with an accumulation region. The grain boundary can act as a tunneling barrier due to the disruption of atomic periodicity at the interface; however, the grain boundary resistance in this case is significantly lower than for the depletion-type interface.

The relationship between the atomic structure of the grain boundary and the electronic properties can be inferred from the direct measurements of grain boundary potential and transport properties by SPM. The topography and potential of the grounded surface are illustrated in Figs. 2(a) and 2(b). The surface is extremely flat with a rms roughness less then 1 nm. Pores with diameters of ~100–200 nm are distributed nonuniformly along the interface, as also reported by other groups.[45] The surface potential measured 50 nm above the surface exhibits a sharp protrusion associated with the grain boundary, Fig. 2(b). The width of the potential feature is ~700 nm and the magnitude is ~20 mV. Note that this potential is significantly smaller than expected for typical $SrTiO_3$ interfaces (~0.5 V) and the width of the observed grain boundary contrast (~700 nm) is significantly larger than the bulk depletion width determined from capacitance measurements (~15 nm).

Strikingly, the sign of the grain boundary potential feature as observed by SSPM is positive, indicative of an accumulation-type grain boundary, which might account for the small value of grain boundary potential. However, from SSPM imaging under applied bias, the grain boundary is unambiguously associated with a potential barrier as illustrated in Figs. 2(c) and 2(d) and, therefore, is of the depletion type, i.e., charged negatively. This discrepancy is due to the

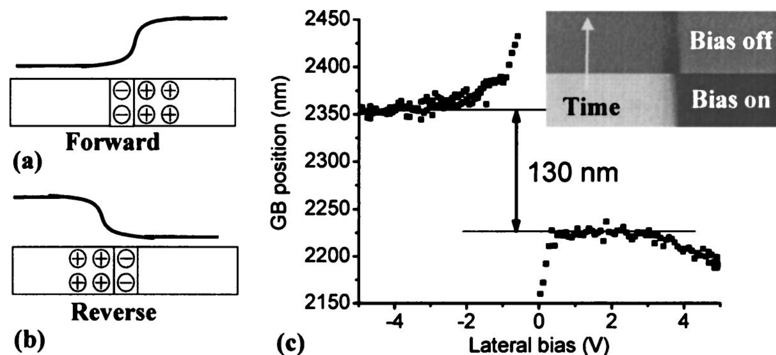

FIG. 4. Potential profile above (a) forward and (b) reverse biased grain boundary illustrating the displacement of center of gravity of potential profile with bias. (c) Bias dependence of grain boundary position. The inset shows the change of the grain boundary potential sign to negative after application of lateral bias due to removal of screening charges [cf. Fig. 2(b)].

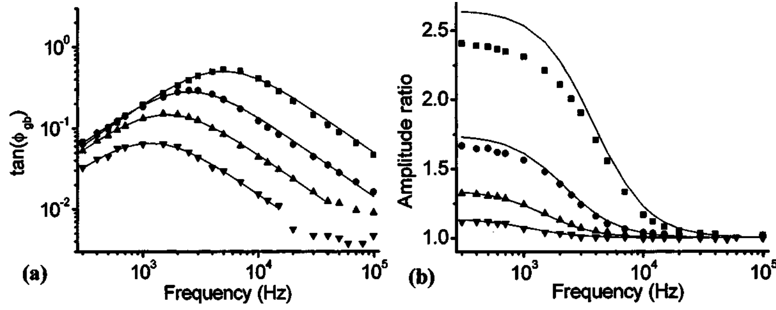

FIG. 5. Frequency dependence of (a) grain boundary phase shift and (b) amplitude ratio in $SrTiO_3$ bicrystal (Model 1). Solid lines on (a) are fits for frequency independent grain boundary resistance and capacitance by Eq. (6), on (b)—calculations by Eq. (13) using data from Table II. Data are shown for circuit terminations 148 Ω(■), 520 Ω(●), 1.48 kΩ(▲), and 4.8 kΩ(▼).

screening by charged adsorbates at the surface-interface junction that results in the widening of the grain boundary potential feature and sign inversion, as reported elsewhere.[30] The adsorbates can be removed by the application of strong lateral electric field across the interface, as illustrated in Fig. 4(c). Similar behavior was observed for ferroelectric surfaces, on which the equilibrium surface potential as observed by SSPM has the sign of the screening charge rather than polarization charge.[31,46] This suggests that surface screening is a universal feature of oxide surfaces in air and great care should be taken in the interpretation of the results of ambient electrostatic SPMs.

B. Direct current transport across the grain boundary

On applying a lateral bias across the surface, a potential drop develops at the grain boundary, indicating its resistive nature [Figs. 2(c) and 2(d)]. To quantitatively determine interface transport properties, a slow triangular bias ramp (2 mHz) is applied across the bicrystal during SSPM imaging. The SSPM image is then the applied bias dependence of interface potential drop. From these data, both potential drop across the interface as a function of lateral bias (voltage characteristic) and the actual potential distribution across the interface can be determined. The voltage characteristics of the interface for different current limiting resistors are shown in Fig. 3(a). The voltage drop across the interface is almost linear for small lateral biases and then saturates, illustrating the decrease of the interface resistance with bias. The maximum observed potential drop across the interface is ~ 1 V; application of higher biases or the use of smaller circuit termination resistors resulted in current flow to the tip and destruction of the latter. For a known circuit termination resistor, R, the current-voltage characteristic of the interface can be reconstructed using Eq. (3) as shown in Fig. 3(b). Reconstructed I-V curves for different circuit terminations coincide with each other and with the I-V curve obtained by direct two probe measurements. This indicates that bulk and contact contributions to the resistance are negligibly small compared to the grain boundary resistance.

Additional information on grain boundary properties can be obtained from the structure of the potential profile under applied bias. Biasing the grain boundary is accompanied by the displacement of the center of mass of the depletion region as illustrated in Figs. 4(a) and 4(b). This displacement from negative to positive breakdown voltage is equal to the depletion width. To analyze the grain boundary position, 256 potential profiles at different biases were extracted and fitted by the Boltzmann function $V(x)=V_0+\Delta V(1+\exp[(x-x_c)/w])^{-1}$, where ΔV is the potential drop at the interface, w is the width of potential profile and x_c is the position of the profile. Figure 4(c) shows the position of the potential profile as a function of external bias from which the displacement is estimated as ~ 130 nm. This value is also very similar to the depletion width determined from a force gradient-distance and force-distance analysis[28] and must be attributed to the Debye length of the screening charges rather than the intrinsic depletion width. Intrinsic grain boundary potential and depletion width can be expected to be determined only under controlled atmosphere or in ultrahigh vacuum environment.

Figures 5(a) and 5(b) show the frequency dependence of interface phase shift and amplitude ratio for different circuit terminations determined by SIM. In the first analysis, phase shift data were fitted by Eq. (6) for a frequency independent R_{gb}, C_{gb} (Model 1); the results are summarized in Table II. Note that the interface capacitance is virtually independent of circuit termination resistance, while interface resistance is smaller for small circuit termination resistances. This behavior is ascribed to the large driving amplitude used in this experiment $(1\ V_{pp})$, which results in the decrease of effective interface resistance due to the nonlinear I-V characteristic of the grain boundary. The effective oscillation amplitude is

TABLE II. Grain boundary properties by Model 1.

R, ohm	R_{gb}, ohm	C_{gb}, 10^{-7} F
148	243.7±3.5	2.14±0.04
520	387.8±4.5	2.15±0.04
1480	510.1±3.0	2.25±0.03
4700	666.3±7.0	2.21±0.04
Impedance spectroscopy	533±0.4	2.94±0.01

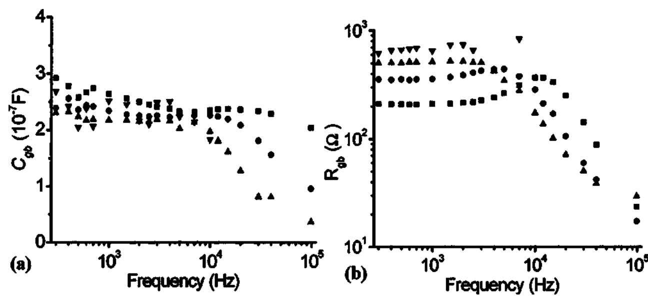

FIG. 6. Frequency dependent interface capacitance (a) and resistance (b) calculated from Eqs. (6) and (7) (Model 2). Data are shown for circuit terminations 148 Ω(■), 520 Ω(●), 1.48 kΩ(▲), and 4.8 kΩ(▼).

larger for small R, resulting in a reduction of effective R_{gb}. This effect can be minimized by imaging in the small signal regime using cantilevers with higher sensitivity.[47] To check the consistency of interface parameters, the frequency dependence of amplitude ratios for different circuit termination resistors is calculated using Eq. (7) and data in Table II as shown in Fig. 6(b). Note the excellent agreement between the measured and calculated values despite the absence of free parameters.

In the second analysis we consider the frequency dependence of interface resistance and capacitance. In this case, Eqs. (6) and (7) are solved at each frequency for R_{gb}, C_{gb} and the resulting values are plotted in Fig. 6. Thus determined capacitance values are relatively frequency independent, while the interface resistance rapidly decreases in the high frequency region. This behavior is because the amplitude ratio is close to unity for high frequencies and small errors in the amplitude ratio and surface potential required for bias correction [Eq. (5)] result in large errors in calculated resistance and capacitance. To summarize, interface resistance can be most reliably determined in the low frequency regime, whereas interface capacitance can be determined both in the low frequency regime (Models 1 and 2) and in the high frequency regime using Model 1 for phase data and known values for circuit termination resistances.

The SIM capacitance-voltage behavior is illustrated in Fig. 7. Here, the phase and amplitude are measured as a function of tip bias at 5 kHz, i.e., in the region where the reliable determination of R_{gb}, C_{gb} is possible. The phase shift-bias dependence is symmetric as a function of bias as illustrated in Fig. 7(a). For the amplitude data, the correction for tip bias and surface bias variation is introduced according to Eq. (5). The symmetric shape of the amplitude-bias curve in Fig. 7(b) with respect to tip bias is indicative of the adequate potential correction. The grain boundary resistance and capacitance calculated from these data for different circuit terminations (Model 2) are shown in Figs. 7(c) and 7(d). Note that the bias dependence of the interface resistance is not sensitive to circuit termination, but is well below the corresponding value determined from the I-V curve due to the large driving amplitude effect. The interface capacitance exhibits a weak bias dependence, which is attributed to the errors in the experimentally measured amplitude ratio. For comparison, the bias and frequency dependence of interface capacitance from conventional C-V measurements using the same oscillation amplitude is shown in Fig. 8(a). SIM data for $R=520\ \Omega$ and 5 kHz (matched resistances) and C-V data for 10 kHz are compared in Fig. 8(b), illustrating the good agreement between the two in the large modulation signal regime. This demonstrates that extrapolation of SIM for small signal amplitudes will allow precise determination of interface parameters.

These results illustrate that application of the SSPM and SIM for the quantification of the interface transport properties is remarkably similar to conventional C-V and four probe impedance spectroscopy measurements. In both cases, care must be taken to minimize the amplitude of the probing voltage to minimize its effect on measured properties. Conventional current-based transport measurements allow significantly higher sensitivity and precision and are capable of measurements in the larger (1 mHz–100 MHz) range. In

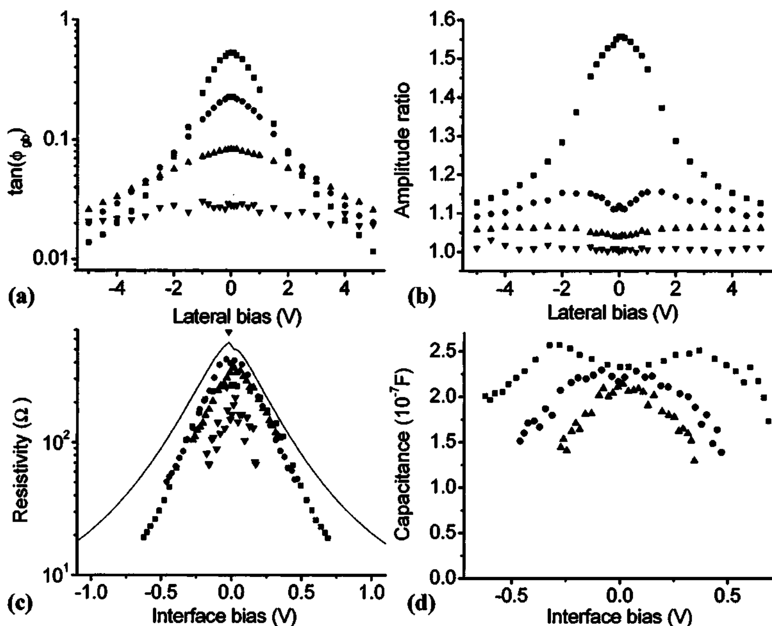

FIG. 7. Lateral bias dependence of (a) interface phase angle and (b) amplitude ratio measured at 5 kHz. Grain boundary bias dependence of (c) grain boundary resistance and (d) capacitance. Solid line on (c) is grain boundary resistance from I-V measurements. Data are shown for circuit terminations 148 Ω(■), 520 Ω(●), 1.48 kΩ(▲), and 4.8 kΩ(▼).

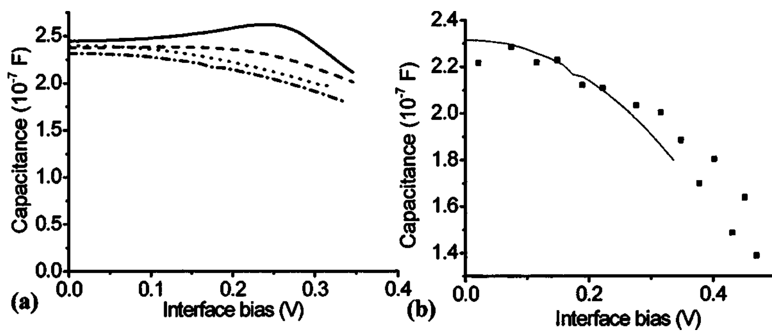

FIG. 8. (a) Bias dependence of interface capacitance at 1 kHz (solid line), 3 kHz (dashed line), 10 kHz (dotted line), and 20 kHz (dash-dot). (b) Bias dependence of interface capacitance from *C-V* measurements at 10 kHz and SIM measurements at 5 kHz and circuit termination of 520 Ω. The frequency and circuit termination values in *C-V* and SIM experiments are matched.

SIM, the frequency range is limited by the bandwidth of the optical detector to ~2–3 MHz; better performance can be expected using alternative detection schemes. Using the calibration and correction procedures described above, SIM and SSPM can provide transport information with ~10%–20% error (primarily due to the cantilever contribution to the signal). The advantage of SIM and SSPM is that these techniques allow spatial localization of microstructural elements with resistive and capacitive behavior, which can be then compared to AFM, optical or electron microscopy images. SIM/SSPM will provide the best results in conjunction with traditional current based transport measurements, so that the global frequency dependent impedance of the system and local behavior of the individual structural element are determined simultaneously.

C. Conductive AFM studies of $SrTiO_3$ interface

SSPM measurements under applied bias unambiguously associate the grain boundary with a high-resistance region which can be associated with a depletion-type space charge layer at the negatively charged grain boundary and a tunneling barrier due to the disruption of atomic periodicity at the accumulation-type grain boundary. To obtain additional information on the interface properties and to establish the origins of the resistive behavior of the interface, we used the single- and two-terminal variants of conductive AFM as discussed in Sec. II C.

Single-terminal c-AFM current image of the grounded bicrystal surface and the corresponding profile perpendicular to the grain boundary are shown in Figs. 9(a) and 9(b). The grain boundary is clearly associated with a low conductivity region, in agreement with the SIM/SSPM transport data. The width of the profile in c-AFM is determined by the depletion width of the grain boundary and imaging conditions such as the rise time of the current amplifier and tip-surface contact area. The average tip-surface current far from the grain boundary is strongly tip and bias polarity dependent and, for the probe used, was 1.34 mA at a tip bias of 1 V. Using the

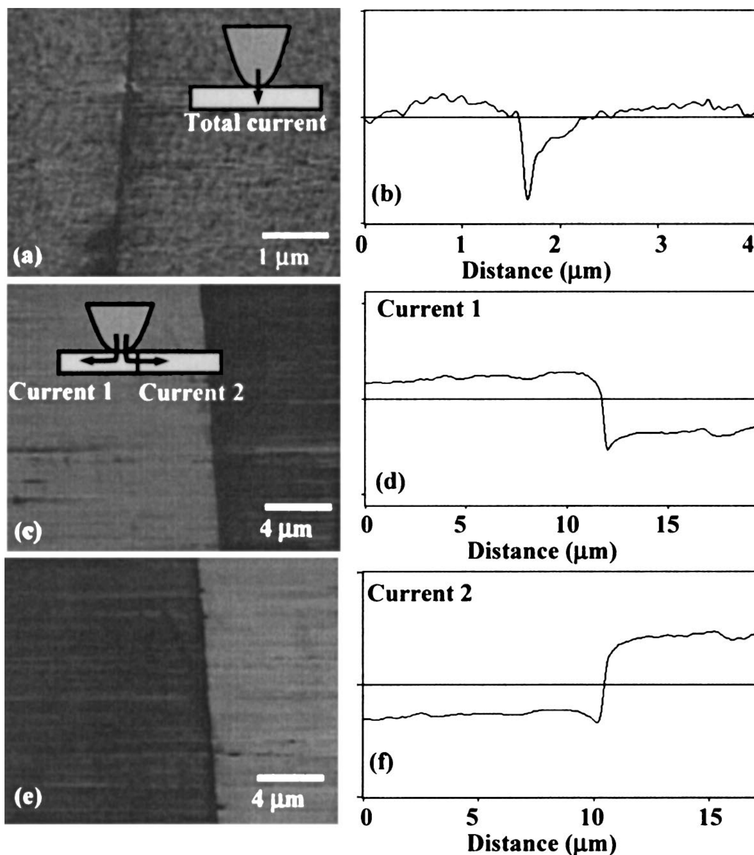

FIG. 9. Current images (a), (c), (e) and current profiles (b), (d), (f) across the $SrTiO_3$ grain boundary in the single terminal (a), (b) and two-terminal measurements (c)–(f). Insets show the schematic of single-terminal (a) and two-terminal (c) setups.

specific resistance value $\rho=0.017\ \Omega\,\mathrm{cm}$ for Nb-doped $SrTiO_3$ (also Ref. 48), the contact radius can be estimated as 18 nm. The width of the grain boundary feature is ~100 nm, so the conductivity is suppressed by ~18% compared to the bulk value. The observed interface width and magnitude are a weighted average of interface and bulk due to the instrumental broadening. If the conductance in the grain boundary region is much smaller than in the bulk and the interface current is zero, the intrinsic depletion width can be estimated as ~18 nm. This is close to the estimation from the measured grain boundary capacitance ($d=22$ nm). At the same time, this value is significantly higher than can be expected for a tunneling barrier formed, e.g., at an accumulation-type grain boundary.

The results of two-terminal measurements of the same interface are illustrated in Fig. 9(c)–9(f). Note the formation of a sharp current step when the tip traverses the grain boundary. The magnitude of the current step is determined by the voltage divider ratio formed by the grain boundary resistance and circuit termination resistance, Eq. (9). The relative current drop at the interface agrees well with that expected from the ratio of grain boundary resistance and the total resistance (0.81 for current 1, 0.73 for current 2, 0.76 expected for $R_{gb}=600\ \Omega$ and $R=1480\ \Omega$).

These results illustrate the huge potential of the c-AFM for interface characterization. The surface screening charge effect on the measurements is minimal; therefore, interface properties can be characterized reliably. These measurements are complicated by the nature of the tip-surface contact, which, until now, has limited the number of successful experiments. Nevertheless, from these results the grain boundary is shown to be associated with a broad (~20 nm) low-conductivity region and thus is unambiguously depletion type. Also, the spatial resolution of two-terminal c-AFM for transport measurements is ultimately limited by a tip-surface contact area on the order of 3–10 nm, and is thus significantly better than that of SSPM under lateral bias (30–300 nm).

V. CONCLUSIONS

The combination of SSPM and SIM can completely determine local static and dynamic transport properties of interfaces; in this case a Σ5 grain boundary in a Nb-doped $SrTiO_3$ bicrystal. Grain boundary potential measured by SSPM is significantly smaller and opposite in sign to the grain boundary potential in the bulk due to screening at a surface-interface junction by mobile adsorbates. In contrast to SSPM on the grounded surface, frequency dependent current measurements are relatively insensitive to the presence of the screening charge. The combination of SSPM on laterally biased surfaces and SIM yields local *I-V* and *C-V* characteristics, interface resistance and capacitance, distinguishing the contributions of the interface from bulk and contacts. Several models for the quantitative analysis of SIM data were suggested and the results were in a good agreement with conventional transport measurements. Finally, conductive AFM was used to directly image the depletion barrier associated with the grain boundary and determine grain boundary resistance. The SPM results directly verify the origins of temperature and frequency dependent electronic transport across atomically abrupt $SrTiO_3$ grain boundaries due to the negatively biased depletion regions at the grain boundaries.[42]

ACKNOWLEDGMENT

D.A.B. acknowledges financial support from MRSEC Grant No. NSF DMR00-79909.

[1] L. L. Hench and J. K. West, *Principles of Electronic Ceramics* (Wiley, New York, 1990).
[2] *Ceramic Materials for Electronics: Processing, Properties, and Applications*, edited by R. C. Buchanan (Dekker, New York, 1991).
[3] M. E. Lines and A. M. Glass, *Principles and Applications of Ferroelectric and Related Materials* (Oxford University Press, Oxford, 1977).
[4] G. H. Haertling, J. Am. Ceram. Soc. **82**, 797 (1999).
[5] J. G. Bednorz and K. A. Muller, Z. Phys. B: Condens. Matter **64**, 189 (1986).
[6] J. M. D. Coey, M. Viret, and S. Von Molnar, Adv. Phys. **48**, 167 (1999).
[7] M. B. Salamon and M. Jaime, Rev. Mod. Phys. **73**, 583 (2001).
[8] A. P. Sutton and R. A. Ballufi, *Interfaces in Crystalline Materials* (Oxford University Press, Oxford, 1995).
[9] L. L. Balcells, J. Fontcuberta, B. Martinez, and X. Obradors, J. Phys. C **10**, 1883 (1998).
[10] M. Ziese, Rep. Prog. Phys. **65**, 143 (2002).
[11] J. Z. Sun and A. Gupta, Annu. Rev. Mater. Sci. **28**, 45 (1998).
[12] H. Hilgenkamp and J. Mannhart, Rev. Mod. Phys. **74**, 485 (2002).
[13] B. Huybrechts, K. Ishizaki, and M. Takata, J. Mater. Sci. **30**, 2463 (1995).
[14] A. Amin and R. E. Newnham, Key Eng. Mater. **66, 67**, 339 (1992).
[15] S. B. Desu, Key Eng. Mater. **66, 67**, 375 (1992).
[16] M. M. McGibbon, N. D. Browning, A. J. McGibbon, and S. J. Pennycook, Philos. Mag. A **73**, 625 (1996).
[17] N. D. Browning, H. O. Moltaji, and J. P. Buban, Phys. Rev. B **58**, 8289 (1998).
[18] F. Ernst, O. Kienzle, and M. Ruhle, J. Eur. Ceram. Soc. **19**, 665 (1999).
[19] N. D. Browning and S. J. Pennycook, J. Phys. D **29**, 1779 (1996).
[20] Z. Zhang, W. Sigle, W. Kurtz, and M. Rühle, Phys. Rev. B **66**, 214112 (2002).
[21] G. Duscher, J. P. Buban, N. D. Browning, M. F. Chisholm, S. J. Pennycook (unpublished).
[22] S.-D. Mo, W. Y. Ching, M. F. Chisholm, and G. Duscher, Phys. Rev. B **60**, 2416 (1999).

[23] R. A. De Souza, J. Fleig, J. Maier, O. Kienzle, Z. Zhang, W. Sigle, and M. Rühle, J. Am. Ceram. Soc. **86**, 922 (2003).
[24] *Scanning Probe Microscopy and Spectroscopy: Theory, Techniques and Applications*, edited by D. A. Bonnell (Wiley, New York, 2000).
[25] M. Nonnenmacher, M. P. O'Boyle, and H. K. Wickramasinghe, Appl. Phys. Lett. **58**, 2921 (1991).
[26] P. M. Bridger, Z. Z. Bandic, E. C. Piquette, and T. C. McGill, Appl. Phys. Lett. **74**, 3522 (1999).
[27] Q. Xu and J. W. P. Hsu, J. Appl. Phys. **85**, 2465 (1999).
[28] S. V. Kalinin and D. A. Bonnell, Phys. Rev. B **62**, 10 419 (2000).
[29] K. Domansky, Y. Leng, C. C. Williams, J. Janata, and D. Petelenz, Appl. Phys. Lett. **63**, 1513 (1993).
[30] S. V. Kalinin and D. A. Bonnell, Nano Lett. **4**, 555 (2004).
[31] S. V. Kalinin and D. A. Bonnell, Phys. Rev. B **63**, 125411 (2001).
[32] S. V. Kalinin and D. A. Bonnell, J. Appl. Phys. **91**, 832 (2002).
[33] *Impedance Microscopy: Emphasizing Solid Materials and Systems*, edited by J. R. Macdonald (Wiley, New York, 1987).
[34] G. Blatter and F. Greuter, Phys. Rev. B **33**, 3952 (1986).
[35] P. De Wolf, J. Snauwaert, L. Hellemans, T. Clarysse, W. Vandervorst, M. D'Olieslaeger, and D. Quaeyhaegens, J. Vac. Sci. Technol. A **13**, 1699 (1995).
[36] A. C. Diebold, M. Kump, J. J. Kopanski, and D. G. Seiler, *Characterization of two-dimensional dopant profiles: status and review*, in Proceedings of the Symposium on Diagnostic Techniques for Semiconductor Materials and Devices, edited by D. K. Shroder, J. L. Benton, and P. Rai-Choudhury (Electrochem. Soc., Pennington, NJ, 1994), pp. 78–96.
[37] P. De Wolf, M. Geva, T. Hantschel, W. Vandervorst, and R. B. Bylsma, Appl. Phys. Lett. **73**, 2155 (1998).
[38] S. V. Kalinin, Ph.D. Thesis, University of Pennsylvania, Philadelphia, 2002.
[39] S. V. Kalinin, G. Duscher, and D. A. Bonnell (unpublished).
[40] N. D. Browning, J. P. Buban, H. O. Moltaji, S. J. Pennycook, G. Duscher, K. D. Johnson, R. P. Rodrigues, and V. P. Dravid, Appl. Phys. Lett. **74**, 2638 (1999).
[41] *Command Reference Manual* (Digital Instruments, Santa Barbara, CA, 2002).
[42] D. A. Bonnell and S. V. Kalinin, Z. Metallkd. **94**, 188 (2003).
[43] N. D. Browning, S. J. Pennycook, M. F. Chisholm, M. M. McGibbon, and A. J. McGibbon, Interface Sci. **2**, 397 (1995).
[44] R. Feidenhans'l, A. Kazimirov, D. M. Smilgies, Q. Jiang, and J. Zegenhagen, Philos. Mag. Lett. **78**, 51 (1998).
[45] E. B. McDaniel, S. C. McClain, and J. W. P. Hsu, Appl. Opt. **37**, 84 (1998).
[46] S. V. Kalinin, C. Y. Johnson, and D. A. Bonnell, J. Appl. Phys. **91**, 3816 (2002).
[47] J. Shin, V. Meunier, A. P. Baddorf, and S. V. Kalinin, Appl. Phys. Lett. (to be published).
[48] K. D. Johnson and V. P. Dravid, Interface Sci. **8**, 189 (2000).